The DOI for this manuscript is doi: 10.1175/2008JPO3810.1

Mesoscale to Submesoscale Transition in the California Current System: Energy Balance and Flux

X. Capet, J.C. McWilliams, M.J. Molemaker, and A.F. Shchepetkin

Institute of Geophysics and Planetary Physics

UCLA, Los Angeles, CA 90095-1567

Revision for *J. Phys. Ocean.* in January 2008

Corresponding author address: Xavier Capet, IGPP/UCLA, 405 Charles E. Young Dr., Los Angeles, CA 90095-1567. E-mail: capet@atmos.ucla.edu

Abstract

This is the last of a suite of three papers about the transition that occurs in numerical simulations for an idealized equilibrium, subtropical, eastern-boundary, upwelling current system similar to the California Current. The transition is mainly explained by the emergence of ubiquitous submesoscale density fronts and ageostrophic circulations about them in the weakly stratified surface boundary layer. Here the high-resolution simulations are further analyzed from the perspective of the kinetic energy (KE) spectrum shape and spectral energy fluxes in the mesoscale-to-submesoscale range in the upper ocean. For wavenumbers greater than the mesoscale energy peak, there is a submesoscale power-law regime in the spectrum with an exponent close to -2. In the KE balance an important conversion from potential to kinetic energy takes place at all wavenumbers in both the mesoscale and submesoscale ranges; this conversion is the energetic counterpart of the vertical restratification flux and frontogenesis discussed in the earlier papers. A significant forward cascade of KE occurs in the submesoscale range *en route* to dissipation at even smaller scales. This is contrary to the inverse energy cascade of geostrophic turbulence, and we demonstrate that it is fundamentally associated with the horizontally divergent (*i.e.*, ageostrophic) velocity component. The submesoscale dynamical processes of frontogenesis, frontal instability, and breakdown of diagnostic force balance are all essential elements of the energy cycle of potential energy conversion and forward KE cascade.

1. Introduction

Wind-driven currents exhibit mesoscale instabilities, and the resulting mesoscale eddies are typically the flow type with the largest kinetic energy (KE) in the ocean (besides the tides). The prevailing dynamical paradigm for the oceanic general circulation encompasses these large- and mesoscale currents together with mixing and dissipation primarily caused by microscale flows (*e.g.,* turbulent boundary layers and breaking internal waves). In this paper and its companions (Capet et al. 2007a and Capet et al. 2007b; here designated as Part I and Part II), we investigate the near-surface submesoscale currents at an intermediate scale — approximately defined by a horizontal scale of $\mathcal{O}(10)$ km, less than the first baroclinic deformation radius; a vertical scale of $\mathcal{O}(10)$ m, thinner than the main pycnocline; and a time scale of $\mathcal{O}(1)$ d, comparable to a lateral advection time for submesoscale feature by a mesoscale velocity — as another potentially important element of the oceanic general circulation. Our purposes are to understand the origins of submesoscale fluctuations, their flow structure and dynamics, and their time-averaged eddy fluxes both spatially and in wavenumber-space as a possible route to energy dissipation at the microscales (Müller et al. 2005).

In Parts I and II a set of computational simulations for an idealized subtropical, eastern-boundary, upwelling current system is analyzed for the emergent submesoscale flows and underlying processes that spontaneously arise once the horizontal grid resolution becomes fine enough. The simulations are integrated to statistical equilibrium for a range of horizontal grid resolutions from $dx = 12$ down to 0.75 km (*i.e.*, cases ICC12 to ICC0; Part I) in an inner domain of size (720 km)^2 embedded within a much larger eastern-boundary current domain in equilibrium with steady wind stress and buoyancy flux and open-ocean lateral boundary fields. The mean alongshore and upwelling currents are unstable and generate vigorous mesoscale eddies. In turn the horizontal strain-rate field from the mesoscale eddies energizes the submesoscale mainly in the surface boundary layer by initiating frontogenesis. This leads to submesoscale frontal instabilities, secondary frontogenesis in the frontal meanders, and coherent vortices. The horizontal wavenumber spectrum shape seems to converge toward $\sim k^{-2}$ power laws for both

velocity and tracers in the submesoscale range. The submesoscale currents have larger Rossby number values than the mesoscale eddies, and they show significant departures from diagnostic force-balance relations. They are highly intermittent with long tails in the Probability Density Functions for buoyancy gradient, vertical vorticity, and vertical velocity, and they exhibit significant skewness in favor of stronger cyclonic vorticity and downward velocity, as typically arises during surface frontogenesis. Submesoscale eddies provide a mean vertical buoyancy flux (*i.e.*, conversion of available potential energy into KE) that acts to restratify the upper ocean as also more generally expected in the presence of frontogenesis.

In this companion paper we analyze the KE spectrum (Sec. 2), as well as the spectral KE balance and flux through the submesoscale wavenumber range (Secs. 3-4); demonstrate the central importance of ageostrophic currents in the forward KE cascade from mesoscale eddies to dissipation at smaller scales (Sec. 4b); interpret the submesoscale energetics (Sec. 5); and in summary present a conceptual model for the flow structures and dynamical processes involved in the submesoscale transition (Sec. 6). The focus of this paper is on the KE balance, with inferences about the associated available potential energy balance (Sec. 5c) pending further clarification of its analysis methodology (Molemaker and McWilliams 2008).

2. Kinetic Energy Spectrum

A defining characteristic of the submesoscale transition is the shallowing of the slope for horizontal wavenumber spectra in the upper ocean in the wavenumber range greater than the mesoscale spectral peak when the grid resolution becomes finer than $\mathcal{O}(10)$ km (Sec. 4 of Part I). One-dimensional (1D) spectra for spatial fluctuations in T, ρ, and $\mathbf{u}_h$ (with the subscript h denoting a horizontal vector) seem to converge towards a power-law regime $\propto k^{-2}$ that extends as far as the dissipation range at high wavenumbers near the grid scale (Fig. 6 of Part I). To set the context for the energy analyses of this paper, Fig. 1 shows two-dimensional (2D) KE spectra as a function of the horizontal wavenumber magnitude, $k = |\mathbf{k}_h|$, after azimuthal integration in wavenumber-space since the fluctuations are approximately isotropic in

$\mathbf{x}_h$ (Part I). The domain used for this spectral analysis (and subsequent ones unless otherwise stated) is (576 km)^2 (*e.g.*, 768^2 grid points in the solution designated ICC0 that has a grid scale of $dx = 0.75$ km; Sec. 2 of Part I). It excludes the "sponge" (*i.e.*, open-boundary damping) and coastal (within 50 km of the shore) regions. The velocity fields have been multiplied by the 2D Hanning window (Jenkins and Watts 1968) prior to applying the Fourier transform. The resulting spectra are then adjusted to compensate for the variance reduction (by a factor 4) due to windowing. 360 instantaneous fields at daily intervals are processed to obtain an average spectrum. This procedure is applied throughout the paper including the cross-spectra in Sec. 3. Spectral analyses of non -periodic fields are unavoidably affected by the artificial periodization procedure. The reduced distortion with the Hanning window and the scale separation between the submesoscale range of interest and the domain size ensure reliability of the computed spectra. Spectral stability *vis a vis* domain size was checked by dividing the diagnostic domain into 4^n sub-pieces (with n=1,2 for ICC0, n=1 for ICC1), computing spectra over each sub-domain and averaging them.

The different simulations converge toward an approximately k^{-2} shape by increasing the energy in the submesoscale range as the resolution increases, in agreement with the 1D spectra shown in Part I. Conversely, the KE spectral level in the mesoscale range remains roughly constant with resolution. Our main focus in the remainder of the paper is on the interpretation of these spectra in dynamical terms. This includes a rationalization of the resolution sensitivity observed over the submesoscale range. We will concentrate on the simulation ICC0 with the highest resolution and widest $\sim k^{-2}$ kinetic-energy spectral range. ICC1 and ICC3 will also be used to investigate resolution sensitivity. In the next section we analyze the spectral energy balance in the submesoscale k range to show how it departs from the simple conception of an inertial-cascade range in either KE or potential enstrophy (*i.e.*, geostrophic turbulence with spectral slopes of -5/3 or -3, respectively; Charney 1971).

3. Kinetic Energy Balance

3a. *Balance Equation*

Consider a point-wise KE balance for the primitive equations:

$$\frac{1}{2}\,\partial_t \mathbf{u}_h^2 \;=\; -\mathbf{u}_h\cdot(\mathbf{u}_h\cdot\boldsymbol{\nabla}_h)\mathbf{u}_h - \mathbf{u}_h\cdot w\partial_z\mathbf{u}_h - \frac{1}{\rho_o}\,\mathbf{u}_h\cdot\boldsymbol{\nabla}_h p + \mathbf{u}_h\cdot\boldsymbol{D}_h + \mathbf{u}_h\cdot\partial_z(\kappa\partial_z\mathbf{u}_h)\,, \quad (1)$$

where the subscript "h" denotes a horizontal vector, and vectors without a subscript are three-dimensional (3D). The right-side terms, respectively, are horizontal and vertical advective energy flux divergences, horizontal pressure work, horizontal mixing implying energy dissipation (left unspecified for now), and vertical mixing that combines wind work and energy dissipation.

We manipulate this balance by spectrally decomposing it with respect to horizontal wavenumber and averaging it with time and also vertically between the level $z = z_0$ and the free surface elevation ζ. This yields

$$\begin{aligned} T \;&=\; \frac{1}{\zeta - z_0}\int_{z_0}^{\zeta} \mathcal{R}e\,\overline{\left[\, -\widehat{\mathbf{u}}_h^*\cdot\widehat{(\,\mathbf{u}_h\cdot\boldsymbol{\nabla})\mathbf{u}_h} \;-\; \widehat{\mathbf{u}}_h^*\cdot\widehat{w\,\partial_z\mathbf{u}_h} \;-\; \frac{1}{\rho_o}\,\widehat{\mathbf{u}}_h^*\cdot\widehat{\boldsymbol{\nabla}_h p} \;+\; \widehat{\mathbf{u}}_h^*\cdot\widehat{\boldsymbol{D}_h} \;+\; \widehat{\mathbf{u}}_h^*\cdot\widehat{\partial_z\kappa\partial_z\mathbf{u}_h} \,\right]}\, dz \\ &=\; \qquad A_h \qquad + \qquad A_v \quad + \qquad P_h \qquad + \quad R \qquad + \qquad V\,, \end{aligned} \quad (2)$$

where the left-side time-tendency T is defined by

$$T \;=\; \frac{1}{2(\zeta - z_0)(t_f - t_i)}\,\int_{z_0}^{\zeta} \mathcal{R}e\,\left[\,\widehat{\mathbf{u}}_h^*\,\widehat{\mathbf{u}}_h\,\right]\Big|_{t_i}^{t_f} dz\,. \quad (3)$$

The symbols in the second line of (2) denote the different contributing terms in the spectral energy balance, and they are aligned under their defining quantity. Each of the terms in (2) is a real-valued function of the horizontal wavenumber, and we will analyze them by azimuthally integrating in k shells. The overbar denotes a time average over the diagnostic interval $t_i \le t \le t_f$. The caret is a horizontal Fourier transform after removing the areal mean and employing a Hanning window function H_w that has the effect of suppressing the advective horizontal boundary fluxes. The symbol $\mathcal{R}e$ denotes the operator that selects the real part. Choosing z_0 of the order of the boundary layer depth (we use $z_0 = -45$ m) in (2) a priori sets an adequate framework

to study upper ocean KE transfers. However, there are several difficulties (other than the windowing distortion; Sec. 2) in implementing and interpreting the diagnosed balance, and these are discussed in the remainder of this section.

The KE changes due to horizontal and vertical momentum advection in A_h and A_v, respectively, are not explicitly computed by ROMS whose 3D advection operator is in flux form. Furthermore, horizontal dissipation[1] occurs as part of the discrete, upstream-biased operator (Shchepetkin and McWilliams 1998). Therefore, we have

$$A_h \; + \; A_v \; = \; F_h^{(u)} \; - \; R \; + \; F_v \; = \; F \, , \tag{4}$$

where $F_h^{(u)}$ and F_v represent the co-spectrum of $\mathbf{u}_h$ with the horizontal and vertical advection components estimated from the flux-form advection scheme. A_h and A_v are diagnosed using centered, second-order, non-dissipative discretization. R can be estimated as $R = F_h^{(u)} - F_h^{(cen)}$, where $F_h^{(cen)}$ is analogous to $F_h^{(u)}$ but with the advective term computed using a centered, second-order, non-dissipative, flux-form scheme. We denote the sum of the conservative, advective, spectral-energy fluxes by F. We verify below that our numerical implementation approximately satisfies (4).

A_h and A_v account for both spectral energy transfer within the domain and also the energy flux through the 3D boundaries. With a tapering window that goes to zero at the lateral edges of the domain, the horizontal energy flux artificially vanishes but the windowing interferes with incompressibility[2]. We judge this effect *a posteriori* to be secondary to the wavenumber transfer in A_h (Sec. 4a). The results for A_v are somewhat sensitive to z_0 in the range 2×10^{-4} rad m^{-1} $\leq k \leq 7 \times 10^{-4}$ rad m^{-1} where vertical advection yields a significant input of kinetic energy but only in the lower portion of the boundary layer and the 10-15 meters below it (Fig. 2). By choosing z_0 deep enough we ensure that the vertical flux through $z = z_0$ is not a dominant effect and that A_v is primarily another means of spectral energy transfer among wavenumbers. Most

[1] In the general case this is σ-level dissipation in ROMS, but our configuration here has a flat bottom, hence horizontal σ-levels.

[2] An alternative approach consists in periodizing the fields to be analyzed by two mirror symmetries; this amounts to performing a Discrete Cosine Transform (DCT; Denis et al. (2002)). However, a DCT also alters the incompressibility properties in two of the quadrants obtained by symmetry.

importantly, the general conclusion about a forward spectral flux of KE (Sec. 4) holds at any depth in the upper ocean, hence is insensitive to the choice of z_0. The location of that forward flux in k is also not very sensitive to z_0 because A_h is only weakly sensitive to z_0 and tends to dominate over A_v.

The horizontal pressure work P_h can be decomposed into 3D pressure work (P) and conversion of potential to kinetic energy (C) using

$$-\frac{1}{\rho_o}\,\widehat{\mathbf{u}_h}^{*}\cdot\widehat{\boldsymbol{\nabla}_h p} \;=\; -\frac{1}{\rho_o}\,\widehat{\mathbf{u}}^{*}\cdot\widehat{\boldsymbol{\nabla} p} \;+\; \widehat{w}^{*}\widehat{b} \tag{5}$$

Only the sum $P_h = P + C$ appears in (2), but to distinguish P from C we separately calculate C by

$$C \;=\; \frac{1}{\zeta - z_0}\int_{z_0}^{\zeta} \mathcal{R}e\left[\,\widehat{w}^{*}\,\widehat{b}\,\right]\,dz\,. \tag{6}$$

If the integral were from top to bottom, P would be identically zero. With our upper-ocean integration interval, P amounts to an energy transfer through the surface $z = z_0$ by pressure work being done on the fluid at this lower bounding surface. Again z_0 was chosen so that the pressure flux out of the control volume could be safely neglected at least in the submesoscale range (Fig. 2). Note however that this term plays an important role to redistribute KE within the upper ocean. In contrast, $C(k)$ is a KE source whose wavenumber integral is unrelated to a boundary flux.

Finally, V is the combination of energy dissipation by parameterized vertical boundary-layer turbulence, vertical diffusive flux through $z = z_0$ (which is small since κ nearly vanishes below the boundary layer, Fig. 2), and generation/dissipation by wind work. Wind work occurs at scales even larger than the mesoscale since the stress field is steady in time and smooth in space. Thus, V is expected to act as dissipation within the submesoscale range.

3b. *Balance Results*

The spectral energy balance (2) is plotted twice in Fig. 3 for the ICC0 simulation in the submesoscale wavenumber ranges, $k \geq 6\times10^{-5}$ rad m^{-1} (top) and $k \geq 3\times10^{-4}$ rad m^{-1} (bottom), in

order to be able to use different ordinate scales. The balance residual (*i.e.*, res $= F+P_h+R+V$) is also shown. The time tendency T is negligible and unable to explain the residual over the submesoscale range. By storing on-line all terms entering the momentum budget over a reduced period of one month, we were able to relate the residual to the momentum discrepancy associated with barotropic mode-splitting in the time integration of ROMS (Shchepetkin and McWilliams 2005), which is not employed in our discrete diagnostic analysis of (2); in practice, this discrepancy is small enough to be neglected.

We now assess the sampling accuracy of these spectral energy balance estimates. As already discussed (Sec. 4 of Part I), the mesoscale component of our simulations has only a few realizations over the one-year analysis period, so it is not fully representative of the range of equilibrium behavior. The submesoscale energy spectrum and its balance terms are therefore likely to vary in quasi-equilibrium with varying mesoscale fields.

To assess the degree of uncertainty in the spectral balance estimate , Fig. 4 shows $F(k)$, $\pm$ its root-mean-square (RMS) fluctuation amplitude (comparable to F itself for $k \leq 3\times 10^{-4}$ rad m^{-1}), together with the sampling uncertainty defined as

$$\pm\, RMS(k)\, \sqrt{\frac{\tau(k)}{t_f - t_i}} \quad = \quad \pm\, \frac{RMS(k)}{\sqrt{k\, U_0\, (t_f - t_i)}}\,,$$

where $\tau(k)$ is the correlation time at wavenumber k. We further consider that $\tau(k)$ is a function of k itself and of an advection velocity U_0 associated with the larger-scale flow, *i.e.*, we suppose that submesoscale activity is intimately tied to its mesoscale environment and therefore evolves on a time scale associated with mesoscale advection. With a typical value $U_0 = 0.1$ m s^{-1} the sampling uncertainty is larger than or comparable to A_h for $k \lesssim 6\times 10^{-5}$ rad m^{-1} (*i.e.*, near the lower-k edge of the submesoscale range). We therefore have excluded this low-k range from Fig. 3 and its discussion. If instead we use a local eddy-turnover time for $\tau(k)$,

$$\tau_{KE}(k) \;=\; [k\, U(k)]^{-1} \;=\; [k^{3/2}\, KE(k)^{1/2}]^{-1} \;\sim\; k^{-\,1/2}\,, \tag{7}$$

leads to a somewhat less stringent wavenumber range restriction. Note finally that, within the analyzed submesoscale wavenumber range, the spectral energy balance is not very sensitive to

the Hanning window function, but the diagnostic energy balance at larger scales does exhibit an important sensitivity (*n.b.*, Hanning-window effects are further discussed in Sec. 4). Thus, we conclude that the submesoscale spectral energy balance in Fig. 3 is credibly estimated.

At all scales a dominant term is the conversion from potential to kinetic energy C. C is robustly positive and should be thought of as the consequence of principally frontogenesis, both as induced by mesoscale straining (Sec. 2 of Part II) and as further enhanced by baroclinic frontal fluctuations (Sec. 4 of Part II). The lower-boundary flux P is a weak sink of KE in the submesoscale range whereas it is a source of KE at mesoscale. F acts as a sink at smaller k and a source at larger k, consistent with a forward transfer of KE from larger scales to smaller ones within this submesoscale range. The decomposition into horizontal and vertical advection components A_h and A_v (Fig. 5) shows important differences between them. F resembles most closely A_h, indicating its dominance over A_v. In particular, the wavenumber range where A_h and F acts as a source is much narrower than that for A_v. In the middle of the submesoscale conservative dynamical regime ($k \approx 2 \times 10^{-4}$ rad m^{-1}), $C > 0$ is balanced primarily by a depletion of energy at that k through $A_h < 0$ and also by the vertical dissipation term $V < 0$; *i.e.,* the main balance is

$$C \approx -A_h - V \,. \tag{8}$$

The possibility of a KE inertial range is rejected since it would be characterized by $F \approx 0$. Dynamical time scales (*i.e.,* eddy-turnover times) are about five days in this regime (Table 1). As k increases the KE sink associated with lateral momentum mixing R progressively becomes comparable to that associated with vertical mixing (V). For $k > 10^{-3}$ rad m^{-1}, both A_h and A_v are positive and become comparable to C. The energy balance here is between conversion and advection as sources and dissipation ($R + V$) as the only sink. In this high-k range the approximate spectral energy balance is

$$C + A \approx -R - V \,, \tag{9}$$

with $C,\, A > 0$ and $R,\, V < 0$. The associated dynamical time scales decrease strongly with k (*e.g.,* at $k = 4 \times 10^{-4}$ and 8×10^{-4} rad m^{-1} in Table 1), reflecting the shape of the energy

spectrum (Fig. 1) as k increases[3]. The eddy turnover time, $\tau_{KE}(k)$ in (7), also has values of a fraction of a day at high k, similar to the other dynamical time scales.

These short submesoscale time scales can be compared with tens of days for the mesoscale regime. Their shortness is consistent with achieving quasi-equilibrium submesoscale energy balance (Fig. 4) even in the presence of slowly varying mesoscale fields. The shortness is also a considerable practical obstacle to detecting submesoscale features from measurements made in the presence of inertia-gravity waves with comparable time scales.

4. Spectral Energy Flux

4a. *Estimation Procedure*

Further insight into the KE transfer is gained by computing the KE spectral flux (*i.e.*, energy transfer rate in k space). This is done by integrating the advective energy-balance terms in k and assuming that the flux vanishes at the highest wavenumber, k_{max}:

$$\Pi(k) \;=\; \int_k^{k_{max}} (\; A_h + A_v \;)\, dk\,. \tag{10}$$

The spectral flux Π is shown in Fig. 6 over the whole k range for several simulations with different horizontal resolution. Due to the open boundaries, some net energy input or output is possible, and we formally split the flux as

$$\Pi = \Pi_t \; + \Pi_b\,,$$

where Π_t represents energy transfers inside the domain and Π_b energy flux through the boundaries. The shapes of A_h and A_v in Fig. 3 imply that $\Pi > 0$ in the high-k range. This positive Π at high k is probably a conservative estimate of a genuine forward energy cascade $\Pi_t > 0$ within the submesoscale range, based on the following considerations. First, if anything, the open boundaries should be a sink of high-k KE because the submesoscale activity is non-existent in

[3]An exception is $\tau_A(k)$ going from 4×10^{-4} to 8×10^{-4} rad m^{-1} in Table 1 because the latter value happens to coincide with the zero crossing in $F(k)$.

the lateral boundary conditions, and it is much weaker beneath the boundary layer (Sec. 4 of Part I); this effect would make $\Pi_b < 0$ and $\Pi_t > \Pi > 0$. The excluded coastal upwelling zone could be both a location of important $\Pi_t > 0$ as well as a source of submesoscale energy for the lateral interior (*i.e.*, contributing to $\Pi_b > 0$ for our analysis domain). To check this we performed a spectral analysis for ICC0 within an even more restricted 512^2 domain that is well separated (by 200 km) from the coast with respect to a typical advective velocity and lifetime of submesoscale structures. The resulting advective flux Π has a similar k dependence as the one represented in Fig. 6 but with a magnitude reduced by $\approx 50\%$. This is at least partly because the submesoscale activity level weakens somewhat with distance from the coast[4]. So we conclude that $\Pi_t > 0$ is not overly based on the behavior in the near-coastal region. Finally, to assess the degree to which our results depend on windowing, the analysis domain for ICC0 was evenly subdivided into four and sixteen sub-domains and an advective flux was computed by averaging the fluxes obtained over each sub-domain (computed in a way analogous to that for the full domain, including Hanning windowing). The stability of Π vis a vis domain size (Fig. 6) indicates the absence of spurious tapering effect.

Independent of resolution, Π changes sign at an intermediate wavenumber k_Π within the submesoscale range since A_h becomes negative at larger k within the submesoscale range. Notice that k_Π changes only slightly with resolution from ICC3 to ICC1 and not between ICC1 and ICC0 ($k_\Pi \approx 2 \times 10^{-4}$ rad m^{-1}), although the magnitude of Π does increase significantly with increasing resolution (Fig. 6). The range with $\Pi < 0$ extends into the mesoscale k range, and it indicates an inverse KE cascade toward larger scales, consistent with geostrophic turbulence. Because of the large sampling uncertainty and the likelihood of a significant Π_b component at larger scales (distorted by the windowing), we hesitate to draw any strong conclusions about the efficacy of a mesoscale inverse KE cascade in our solutions, although our results indicate it does occur to some degree (in agreement with the more reliable estimate by Klein et al. (2008) for a periodic domain).

[4]The same is true for the mesoscale activity both in our simulations and more generally in eastern-boundary currents (Marchesiello et al. 2003).

4b. *Ageostrophic Velocity and KE Flux*

We now assess the degree to which balanced and unbalanced parts of the flow (Sec. 5 of Part II) contribute to the submesoscale forward kinetic energy cascade. For this purpose we make a Helmholtz decomposition of the horizontal velocity into a horizontally non-divergent part and its divergent residual:

$$\begin{aligned} \mathbf{u} \;&=\; \mathbf{u}_h \,+\, w\,\hat{\mathbf{z}} \;=\; \mathbf{u}_{hr} \,+\, (\mathbf{u}_{hd} \,+\, w\,\hat{\mathbf{z}})\,, \\ &\boldsymbol{\nabla}_h \cdot \mathbf{u}_{hr} \;=\; 0 \quad \text{and} \quad \hat{\mathbf{z}} \cdot \boldsymbol{\nabla}_h \times \mathbf{u}_{hd} \;=\; 0\,. \end{aligned} \tag{11}$$

The geostrophic velocity is

$$\mathbf{u}_{hg} \;=\; \frac{1}{\rho_0 f_0}\,\hat{\mathbf{z}} \times \boldsymbol{\nabla}_h p\,,$$

so its velocity is horizontally non-divergent. Hence it is excluded from being part of $\mathbf{u}_{hd}$ and must be entirely contained within $\mathbf{u}_{hr}$. However, a higher-order diagnostic force balance (*e.g.*, gradient-wind balance) can be part of $\mathbf{u}_{hd}$ as well as $\mathbf{u}_{hr}$.

KE spectra associated with this decomposition are plotted in Fig. 7. It is clear that the largest contribution is from $\mathbf{u}_{hr}$, hence possibly from $\mathbf{u}_{hg}$, even extending to high wavenumbers. In contrast, the contribution from $\mathbf{u}_{hd}$, even when added to the ageostrophic vertical velocity contribution, is relatively small. This holds even though there are important local breakdown events for diagnostic force balance (Figs. 18-20 of Part II). The ageostrophic fraction is relatively smaller in the mesoscale range, but it is still small in the submesoscale range.

By analogy with (10), we define the spectral KE flux Π_{hr} associated with only the horizontally non-divergent velocity (*i.e.*, based on calculated A_h in (2) with $\mathbf{u}_h$ replaced by $\mathbf{u}_{hr}$). Π_{hr}, Π, and their difference (*i.e.*, the energy flux involving the vertical and horizontally divergent part of the flow) are plotted in Fig. 8. Π_{hr} almost entirely lacks the forward energy cascade at high k that occurs in $\Pi > 0$, although it does account for the greater part of the $\Pi < 0$ behavior at low k. Thus, the divergent, ageostrophic flow component is essential for the submesoscale forward KE cascade, even though it represents only a small fraction of the velocity variance.

5. Discussion of Submesoscale Energetics

5a. *Resolution Dependence*

As already mentioned in Sec. 2, the KE spectra for our different solutions strongly suggest convergence with resolution for KE (also Fig. 7 of Part I and the related discussion). This is in apparent contradiction with the fact that the total potential energy conversion, $\int C\,dk$, significantly increases with resolution (*i.e.*, a 30% increase from ICC1 to ICC0 and nearly a doubling from ICC3 to ICC0; Fig. 9), because of additional contributions to C in the expanding wavenumber range where frontogenesis is occurring. The reconciliation is because a convergence of $V + C$ occurs even as V and C each continues to increase with Δx. This is shown in Fig. 10, where the vertical dissipation V balances the extra energy source from conversion C. This compensation is reminiscent of that for the heat balance within the boundary layer where increased advective vertical heat flux divergence with resolution is balanced by an increase in vertical mixing (Sec. 7 of Part I). The limiting magnitude of $V + C$ is probably dependent on our parameterized vertical mixing scheme (KPP), although the presence of an advective KE forward flux seems robust *vis a vis* boundary layer parameterization (Molemaker et al. 2007; Klein et al. 2008)[5].

Figure 9 (top) shows that the total amount of horizontal dissipation has also approximately converged by $\Delta x = 0.750$ km, since the small k values of $-\int_k R\,dk$ are nearly the same for simulations ICC1 and ICC0. However, the horizontal dissipation range is displaced toward higher k when resolution increases. At the finest resolution the net conversion, $C + V$ in Figs. 9 (bottom panel) and 10, still overlaps in k with the horizontal dissipation range to some extent, but R is compensated there almost entirely by the advective flux F[6]. This means that our sim-

[5]In Molemaker et al. (2007) and Molemaker and McWilliams (2008), the high horizontal resolution allows for a lateral shear instability that limits the frontogenetic scale. At even larger k, $C \approx 0$, and a forward energy-cascade inertial range develops with KE and available potential energy spectra $\sim k^{-5/3}$. This differs from our simulations where the frontal scale has not converged with resolution, and the dominant frontal instability type is baroclinic (Sec. 4 of Part II). In Klein et al. (2008) a baroclinically-unstable, upper-ocean jet yields an advective, forward KE flux within the submesoscale range in the absence of atmospheric forcing or a boundary-layer mixing parameterization.

[6]The mismatch between the F and R curves in ICC0 for $k \geq 10^{-3}$ rad m^{-1} arises because the pressure flux

ulations are approaching a scale-separation between the net KE injection by potential-energy conversion and the lateral dissipation. Therefore, it seems reasonable to conclude that the amplitude of the forward KE cascade (the maximum value of $\Pi > 0$ in Fig. 9 (top) has nearly converged and that a plateau for Π will emerge with a further resolution increase. If so, then the spectrum slope should shallow towards and energy inertial-range shape, $\sim k^{-5/3}$. Solutions at even finer resolution would be needed to verify these points.

5b. *KE Spectral Slope*

The KE spectrum for ICC0 (Sec. 2) is $\sim k^{-2}$ across the resolution range for our simulations, although the energy balance discussion in Sec. 5a suggests that this wavenumber range may be nearing its end at our highest resolution. Whether or not this is the case, the spectral balance analysis demonstrates that classical inertial range theories developed for homogeneous 3D or 2D and geostrophic turbulence do not apply within our submesoscale range. Most importantly, the spectral budget (Sec. 3) shows that KE injection occurs over a wide k range. Following Klein et al. (2008) and keeping in mind that ageostrophic velocity variance is small (Sec. 4b), the surface KE spectral shape may be seen in the light of surface quasigeostrophy theory (SQG). In SQG surface KE does not have an inertial range (Capet et al. 2008), but it nevertheless does have a $\sim k^{-5/3}$ spectral shape. This is because the surface buoyancy does have an inertial range, and its power spectrum is by definition identical to that for surface KE. An alternative interpretation compatible with a $\sim k^{-2}$ shape would emphasize the presence of horizontal velocity near-discontinuities in relation with frontogenesis near the ocean surface (Boyd 1992). Instances of such discontinuities associated with the density fronts are seen in Fig. 15 of Part II.

P is also increasingly effective at transferring energy below the boundary layer. This mismatch disappears if one integrates deeper, *e.g.*, taking z_0 = 60 m.

5c. *Total Energy Budget*

A remaining issue is the identification of the larger-scale energy source that is tapped into by the increasingly effective submesoscale-driven dissipation in the upper ocean. Eastern boundary systems such as our ICC have a leading order energy balance between wind forcing (a source) and outward boundary flux (a sink) (Marchesiello et al. 2003; Auad et al. 1991) which makes it difficult to track down the effects of comparatively small changes in dissipation. Therefore we limit ourselves to a qualitative discussion.

Computing the wind work in a way that is consistent with our spectral-balance estimates, we find values around 8×10^{-6} m^3 s^{-3}, *i.e.,* a depth-integrated energy input of around $W = 1.8 \times 10^{-7}$ m^2 s^{-3} into the upper layer above z_0. The changes in W with resolution are below 6% of W, *i.e.,* they are most likely within the estimation uncertainty. Most importantly we find $W_{ICC0} < W_{ICC3} < W_{ICC1}$. This and the fact that the wind-work is confined to the lowest wavenumbers (because the wind field is quite smooth) indicate that the wind work does not directly influence the KE balance at the submesoscale.

On the other hand, the wind (or some other form of sustained energy input) is essential to the maintenance of submesoscale activity. [7] In fact the changes in the KE balance with resolution due to increasing potential energy conversion imply an accompanying change in the potential energy balance where the conversion is an energy sink. This sink has to be accommodated somehow by an increased source. Without getting into the details of the potential energy balance here, the boundary-layer heat balance (Sec. 7 of Part I) provides a useful guide to what this source must be. As resolution increases the increase in restratifying vertical heat and buoyancy fluxes associated with submesoscale frontogenesis is counteracted by increased vertical turbulent flux acting to diminish the upper-ocean stratification, with the net result being only a moderate increase in stratification of the mean state. This enhanced mixing within the boundary layer is an added source of potential energy.

[7] If wind stress is shut off in our solutions, rapid depletion of submesoscale variance and restratification of the previously mixed surface layer occur over a period of days, whereas mesoscale variability persists over many months. A similar result is shown in Molemaker et al. (2007) for the spin-down of a vertically-sheared flow.

Because the integrated energy input by surface buoyancy fluxes does not change appreciably with resolution in our solutions these do not provide an appreciable source of energy for the submesoscale. This may not be the case in solutions forced by atmospheric fluxes with synoptic variability, because then the restratification tendency associated with submesoscale activity would translate into SST and air-sea heat flux changes with resolution.

Finally the increased, larger-scale energy source may also come from increased boundary fluxes on the scale of the regional circulation. Indeed the pycnocline structure for the incoming flow is approximately that of the ICC12 simulation with $dx = 12$ km, *i.e.*, somewhat less stratified and with higher potential energy in comparison with the horizontal interior region in the ICC0 simulation with $dx = 0.75$ km (Sec. 7 of Part I).

This indicates that the potential energy sink by submesoscale conversion in the upper ocean is balanced by a combination of lateral boundary flux and vertical mixing. We expect the former source to be associated with small k because of the smooth boundary data. The latter is also acting at small k, as we have verified by computing $\widehat{\rho}^* \cdot \widehat{\partial_z \kappa \partial_z \rho}$ (it is intuitively consistent with a large scale increase of upper-ocean stratification due to the submesoscale transition). This would imply a forward potential energy cascade to connect to the submesoscale conversion sink[8].

5d. *Large-Scale Energy Depletion by Submesoscale Activity*

We can compute several estimates that illustrate the significance of the submesoscale energy flux cascade for the larger-scale dynamics. First, the wind work can be compared to the increment in KE dissipation associated with submesoscale activity, *i.e.*, $\epsilon_{sub} = -\int [\, (V+R)_{ICC0} - (V+R)_{ICC3} \,]\, dk$, the added dissipation when going from 3 to 0.750 km in resolution. The

[8] Available potential energy is the dynamically relevant component of potential energy, and its balance is closely related to the buoyancy variance balance (Winters et al. 1995). We have verified that the advective analog of Π in the latter balance,

$$\tilde{\Pi}(k) \;=\; -\int_k^{k_{max}} \left\{ \frac{1}{\zeta - z_0} \int_{z_0}^{\zeta} \mathcal{R}e \, \overline{\left[\, \widehat{b}^* \, (\, \widehat{\mathbf{u}_h \cdot \boldsymbol{\nabla}) b} \,\right]} \, dz \right\} dk \,,$$

does robustly show a forward spectral flux in our simulations.

ratio ϵ_{sub}/W is about 0.05. Although small this number suggests that wind energy dissipation associated with frontal activity is probably not unimportant for the surface-layer energetics.

Second, a decay time scale T_d for the mesoscale depletion is defined by the ratio of the total energy associated with the surface mesoscale velocity — say, $2 \times \int_{10^{-5}}^{6\times10^{-5}} KE\, dk \approx 10^{-2}$ m^2 s^{-2}, where the factor of two accounts for available potential energy, assuming approximate energy equipartition (Charney 1971) — by the energy dissipation associated with the submesoscale, say $\epsilon = -\int_{6\times10^{-5}}^{\infty}(R+V)\, dk \approx 1.2\times10^{-8}$ m^2 s^{-3} (for ICC0). It yields $T_d \approx 11$ days, which is comparable to or even shorter than a typical mesoscale eddy-turnover time. However, this estimate is based on upper-ocean quantities, and there is significant mesoscale energy beneath $z = z_0$ but not much submesoscale-induced dissipation (*e.g.*, Fig. 2 and Sec. 4 of Part I). This suggests that submesoscale-induced dissipation would act like a top-boundary frictional process and require a mesoscale vertical energy flux (*e.g.*, by pressure work) to redistribute mesoscale energy. Taking into account that submesoscale is mostly confined within a 30-40 m layer whereas mesoscale energy spreads at least within the upper 200 m yields a somewhat longer mesoscale energy depletion time scale $T_d \approx 80$ days.

Third, an "effective eddy viscosity" provided by the submesoscale energy flux acting on the mesoscale reservoir can be estimated in two different ways. If one assumes the flux arises primarily from mesoscale horizontal shear, a natural scale estimate is

$$\nu_h^{(eff)} = \frac{\epsilon}{<(\boldsymbol{\nabla} u')^2>},$$

where the prime indicates a low-pass filtering that selects the mesoscale fluctuations (Sec. 6 of Part I) and ϵ is the dissipation of energy occurring in submesoscale regime defined above. This yields $\nu_h^{(eff)} \approx 80$ m^2 s^{-1} for ICC0. An alternative is an effective vertical eddy viscosity based on the mesoscale vertical shear,

$$\nu_v^{(eff)} = \frac{\epsilon}{<(\partial_z u')^2>}.$$

Because mesoscale currents are approximately in thermal-wind balance, the denominator can be replaced by $g/(\rho_0\, f)\ <(\boldsymbol{\nabla}\rho')^2>$. The result is $\nu_v^{(eff)} \approx 10^{-2}$ m^2 s^{-1}. (For the coarser-grid

simulation ICC3, analogous eddy diffusivity estimates are smaller by a factor of about two.) Both these diffusivity values are much smaller than their mesoscale counterparts, which are the effective horizontal and vertical eddy viscosities corresponding to the mesoscale effect on the mean flow, whose approximate magnitudes are 10^3 and 10^{-1} m^2 s^{-1}, respectively (Gent et al. 1995). Thus, although the direct effect of the submesoscale on the mean currents is smaller than the mesoscale effect, the submesoscale effect is likely to be important for mesoscale currents (with their much larger shears than the mean currents').

5e. *Observational Comparisons*

It is becoming increasingly evident that the upper-ocean KE spectrum derived from satellite measurements is much shallower than expected from geostrophic turbulence theory. Le Traon et al. (2008) find $\sim k^{-5/3}$ for the velocity spectrum in three regions with energetic mesoscale activity. Although this has appreciable estimation uncertainty and is only shown for scales down to 15 km, it does tend to support the presence of energetic small-mesoscale and submesoscale activity in the upper ocean.

The actual role of this activity in terms of energy transfer is difficult to assess from observations. For several regions of the South Pacific, a forward energy cascade range is shown by Scott and Wang (2005). However it arises from altimetry measurements of sea level, hence surface geostrophic velocity. Furthermore their $\Pi > 0$ range extends to much lower wavenumbers of $k \approx 5 \times 10^{-5}$ rad m^{-1} compared to our lower-limiting value of $k \approx 3 \times 10^{-4}$ rad m^{-1}, and the magnitude of $\Pi > 0$ is at a level of about a quarter of the magnitude of the $\Pi < 0$ values at larger scales. Thus, it is unclear if the forward cascade present in these observations occurs for the same reasons than in our simulations.

5f. *Summary of Submesoscale Energetics*

The KE in the submesoscale range is generated primarily by potential energy conversion C. The cause of the potential energy conversion is transformation of mesoscale energy into the submesoscale regime through frontogenesis initially induced by mesoscale straining (Secs. 2-3 of Part II) and reinforced by frontal instabilities dominated by baroclinic energy conversion (Sec. 4 of Part II). The associated KE input occurs mostly within the submesoscale k range, and part of it is further transferred to smaller scales by advection F in a forward energy cascade (*i.e.*, $\Pi > 0$) that fundamentally involves the ageostrophic flow. At highest resolution KE is dissipated primarily by vertical sub-grid scale eddy diffusion V. At smaller wavenumbers abutting the mesoscale range, the KE spectral flux is in the inverse sense (*i.e.*, $\Pi < 0$), consistent with the expectations of surface quasigeostrophic turbulence (Capet et al. 2008), and there may also be an increase due to mesoscale KE flux through the open boundaries. This energy balance maintains the relatively shallow submesoscale KE spectral shape $\propto k^{-2}$.

In the available potential energy balance, we infer that the increase of C with finer resolution (a loss) is balanced by an increase in vertical mixing work in the surface boundary layer (a gain), as well as probably an increase in the lateral boundary flux at the regional scale. A forward advective flux of available potential energy must be connecting the sources at low k and the sink C at high k, and a similar spectral balance occurs for buoyancy variance.

6. Discussion of Submesoscale Structure and Dynamics

In this suite of three papers we analyze the submesoscale transition in numerical simulations of an idealized subtropical, eastern-boundary, upwelling current system with increasingly finer horizontal grid resolution. In addition to the mesoscale eddies that arise from a primary instability of the alongshore, wind-driven currents, significant energy is transferred into submesoscale fronts and vortices in the upper ocean. The submesoscale currents arise through surface (primary) frontogenesis growing off upwelled cold filaments that are pulled offshore and strained

in between the mesoscale eddy centers. In turn some submesoscale fronts become unstable, and a secondary stage of frontogenesis takes place in the vicinity of the developing submesoscale meanders. Such instabilities ultimately lead to the formation of small scale filaments and roll-up vortices, or they stabilize at finite amplitude probably under the influence of mesoscale strain. Submesoscale motions have much larger vertical vorticity, vertical velocity, and horizontal density gradients than their parent mesoscale, and these fields exhibit substantial intermittency and skewness (favoring cyclonic vorticity and downward velocity). The submesoscale horizontal currents approximately satisfy geostrophic balance, but regions with strong vorticity have a significant cyclostrophic force, and even the more general diagnostic force balance fails near strong fronts and during episodes of vigorous frontal instability. Both primary frontogenesis and frontal instability (through secondary frontogenesis) involve a strong vertical eddy buoyancy flux that acts to restratify the upper ocean and convert potential energy to KE. This in turn leads to a forward KE cascade toward microscale dissipation.

On the basis of our simulations, we presently understand the place of the submesoscale regime transition in the general circulation as depicted in Fig. 11. In a broad sweep the submesoscale receives energy from the mesoscale and transmits it to even finer scales where the influences of rotation and stratification weaken and the turbulence approaches the classical 3D isotropic regime *en route* to dissipation. More precisely, the principal mode of energy transfer into the submesoscale in our simulations involves a downscale flux of available potential energy that feeds the conversion process from potential energy to KE. Frontogenesis — initiated by mesoscale straining and reinforced by submesoscale instability in the upper ocean — is consistent with this energy pathway. The present simulations are too limited in resolution to directly characterize the anticipated 3D isotropization process but both frontogenesis and submesoscale instability should provide a route to dissipation.

The integrated potential energy conversion, $\int C\,dk$, will continue to increase with model resolution as long as frontogenesis continues toward smaller scales and the dominant frontal instability type has $\overline{wb} > 0$ (as in our simulations; Sec. 4 of Part II). In our highest-resolution

case (ICC0 with $\Delta x = 750$ m), the frontogenetic C is about four times bigger than the frontal instability C (Fig. 14 of Part II), and the vigor of the frontal instability rapidly increases as the resolution is enhanced (Fig. 4 of Part I). The ageostrophic KE spectrum can be extrapolated in k to intersect the extrapolated geostrophic spectrum (Fig. 7) at a scale of $k^{-1} \approx 250$ m. This suggests that the cross-frontal scale will be arrested at $\mathcal{O}(100)$ m by sufficiently vigorous submesoscale instabilities, including both horizontally meandering ones fed by potential energy conversion with $P\ K_e \propto \overline{wb} > 0$ (*i.e.,* baroclinic and anticyclonic-ageostrophic instability types; Sec. 4 of Part II) or, more likely, some other types that will prevent further increase of C: centrifugal instability fed by the negative potential vorticity generated near down-wind fronts (Sec. 3 of Part II); Kelvin-Helmholtz instability fed by strong submesoscale vertical shear at the base of the boundary layer; or a stronger lateral shear instability.

In our solutions a conversion increase with resolution may not have a major impact on the submesoscale forward advective KE flux Π given the compensation between C and V (vertical dissipation) demonstrated in Sec. 5a. Whether or not this is the case, we expect Π to become approximately independent of k (*i.e.,* A will be zero) for a resolution somewhere between that of ICC0 and ≈ 100 m (when $\int C\,dk$ will cease to increase, as explained above). In this conceptual picture there is no obvious generation of, nor coupling to, inertia-gravity waves, although unlike the ocean our simulations lack an independent source for such waves and so may underrepresent their importance. Sorting out the energetic functioning of the system at higher resolution, and exploring its sensitivity *vis a vis* vertical dissipation parameterization and presence of synoptic scales in the forcing (as a source of inertial oscillations, inertia-gravity waves but also as a way to let frontal processes produce net restratification) open important follow-ups to this study.

Our simulations indicate several important roles for submesoscale currents that need to be parameterized in more coarsely resolved models. These include an enhanced vertical restratification flux in the upper ocean (with the consequence of reducing the turbulent boundary layer thickness; Sec. 7 of Part I) and an enhanced route to dissipation through potential energy con-

version and forward KE cascade. A prototype parameterization has recently been proposed by Fox-Kemper et al. (2007) that attempts to include the former. Although the underlying principles are quite generic, its calibration relies so far on the simple case of a mixed layer front that restratifies as it develops submesoscale instabilities. Our simulations could provide a more complete testbed for such parameterization ideas, but first a better sense is needed of whether the submesoscale transition is widespread in the ocean. There are limited observations that suggest it is so, especially in the upper ocean (Sec. 8 of Part I). Further measurements are needed, of course, and further modeling studies can be useful. An example of the latter is an investigation of the turbulent equilibrium dynamics of Eady's flow with a much deeper vertical structure, absence of well-mixed vertical boundary layers, and horizontal homogeneity (Molemaker et al. 2007). In these simulations an unambiguous demonstration is made of a total (kinetic plus potential) energy forward cascade as the final step *en route* to dissipation.

Acknowledgments The authors greatly appreciate inputs to this research from Patrice Klein, Lien Hua, Guillaume Lapeyre, Rob Scott, Baylor Fox-Kemper, Raffaele Ferrari, Leif Thomas and three anonymous reviewers. We acknowledge support by the ONR grants N00014-04-1-0401 and N00014-05-10293 and NSF grants OCE-0221177 and OCE-0550227. Many of the computations were made at the National Center for Supercomputing Applications.

References

Auad, G., A. Pares-Sierra, and G. K. Vallis, 1991: Energetics and diagnostics of a model of the circulation in the California Current System. *J. Phys. Oceanogr.*, **21**, 1534–1552.

Boyd, J. P., 1992: The energy spectrum of fronts: Time evolution of shocks in Burgers' equation. *J. Atmos. Sci.*, **49**, 128–139.

Capet, X., P. Klein, B. L. Hua, G. Lapeyre, and J. C. McWilliams, 2008: Surface kinetic energy transfer in SQG flows. *J. Fluid Mech.*, in revision.

Capet, X., J. C. McWilliams, M. J. Molemaker, and A. Shchepetkin, 2007a: Mesoscale to submesoscale transition in the California Current System: Flow structure and eddy flux. *J. Phys. Oceanogr.*, in press.

— 2007b: Mesoscale to submesoscale transition in the California Current System: Frontal processes. *J. Phys. Oceanogr.*, in press.

Charney, J. G., 1971: Geostrophic turbulence. *J. Atmos. Sci.*, **28**, 1087–1095.

Denis, B., J. Côté, and R. Laprise, 2002: Spectral decomposition of two-dimensional atmospheric fields on limited-area domains using the discrete cosine transform (DCT). *Mon. Wea. Rev.*, **130**, 1812–1829.

Fox-Kemper, B., R. Ferrari, and R. Hallberg, 2007: Parameterization of mixed layer eddies. I: Theory and diagnosis. *J. Phys. Oceanogr.*, submitted.

Gent, P. R., J. Willebrand, T. J. McDougall, and J. C. McWilliams, 1995: Parameterizing eddy-induced tracer transports in ocean circulation models. *J. Phys. Oceanogr.*, **25**, 463–474.

Jenkins, G. M. and D. G. Watts, 1968: *Spectral Analysis and its Applications*. Holden-Day, 525 pp.

Klein, P., B. L. Hua, G. Lapeyre, X. Capet, S. Le Gentil, and H. Sasaki, 2008: Upper ocean turbulence from high 3-D resolution simulations. *J. Phys. Oceanogr.*, in press.

Le Traon, P. Y., P. Klein, B. L. Hua, and G. Dibarboure, 2008: Do altimeter wavenumber spectra agree with interior or surface quasi-geostrophic theory? *J. Phys. Oceanogr.*, in press.

Marchesiello, P., J. C. McWilliams, and A. Shchepetkin, 2003: Equilibrium structure and dynamics of the California Current System. *J. Phys. Oceanogr.*, 753–783.

Molemaker, M. and J. McWilliams, 2008: A complete energy budget with a local available potential energy density. *J. Fluid Mech.*, submitted.

Molemaker, M., J. McWilliams, and X. Capet, 2007: Submesoscale route to dissipation in an equilibrium Eady flow. *J. Fluid Mech.*, submitted.

Müller, P., J. C. McWilliams, and M. J. Molemaker, 2005: Routes to dissipation in the ocean: The 2D/3D turbulence conundrum. *Marine Turbulence: Theories, Observations and Models*, H. Baumert, J. Simpson, and J. Sundermann, eds., Cambridge University Press, 397–405.

Scott, R. and F. Wang, 2005: Direct evidence of an oceanic inverse kinetic energy cascade from satellite altimetry. *J. Phys. Oceanogr.*, **35**, 1650–1666.

Shchepetkin, A. and J. C. McWilliams, 1998: Quasi-monotone advection schemes based on explicit locally adaptive dissipation. *Mon. Wea. Rev.*, **126**, 1541–1580.

— 2005: The Regional Oceanic Modeling System: A split-explicit, free-surface, topography-following-coordinate ocean model. *Ocean Modelling*, **9**, 347–404.

Winters, K. B., P. N. Lombard, J. J. Riley, and E. A. D'Asaro, 1995: Available potential energy and mixing in density-stratified fluids. *J. Fluid Mech.*, **289**, 115–128.

List of Figures

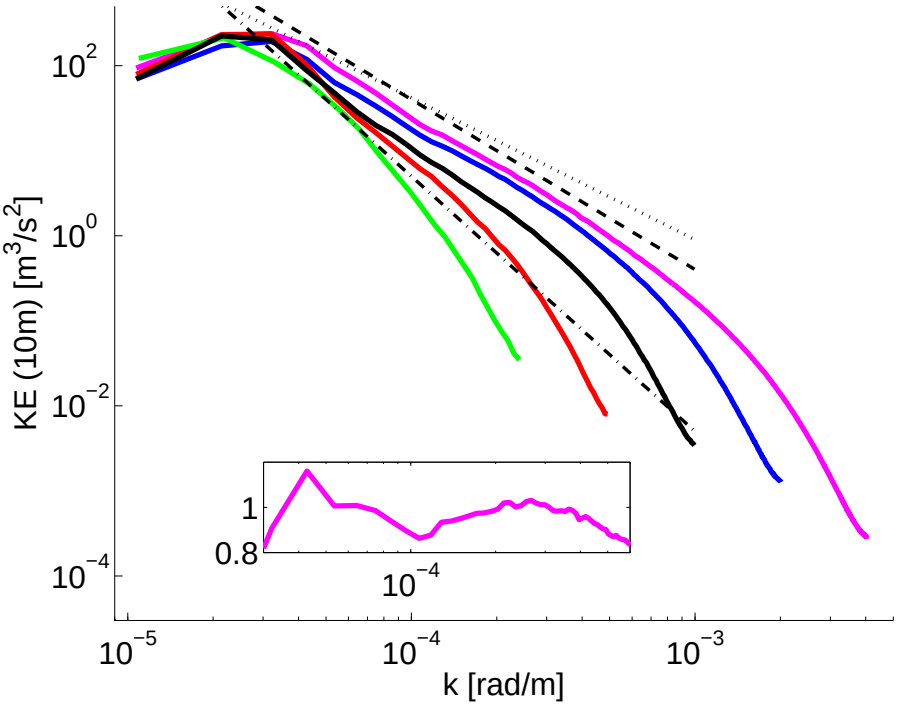

Figure 1: KE spectra for the horizontal velocity $\mathbf{u}_h$ fluctuations at 10m depth as a function of horizontal wavenumber magnitude, $k = |\mathbf{k}_h|$; *i.e.*, the 2D spectrum is azimuthally integrated in k shells. The five solid lines correspond to spectra for the different simulations with the wavenumber range increasing from ICC12 to ICC0 (*i.e.*, horizontal grid scale decreasing from 12 to 0.75 km; Sec. 2 of Part I, Sec. 2). For comparison the straight lines indicate -5/3 (dotted), -2 (dashed), and -3 (dot-dash) spectrum slopes. The spectra are time averaged. The ICC0 spectrum multiplied by k^2 is plotted in the inset with a linear ordinate scale over the indicated intermediate k range.

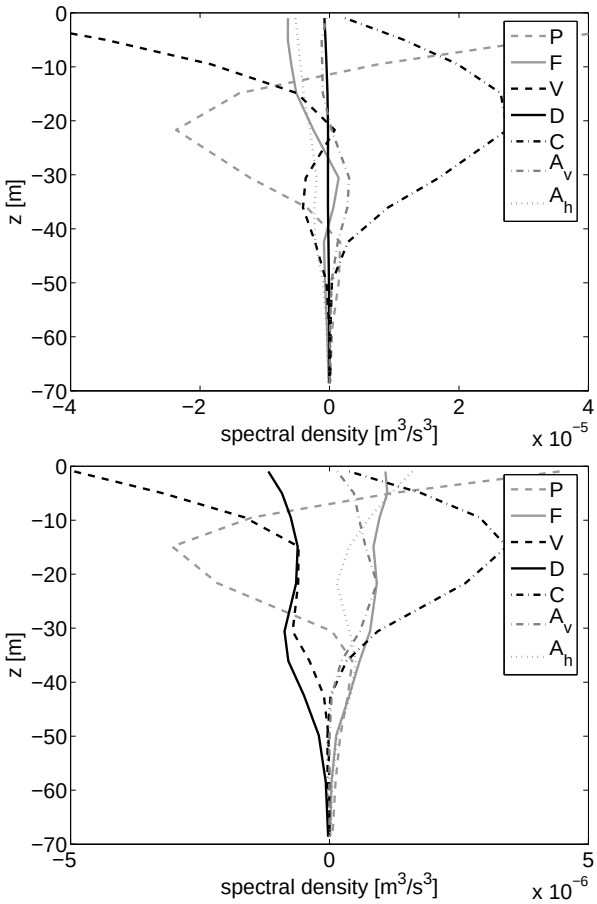

Figure 2: Integrands in the spectral energy balance (2) as a function of depth for $k = 4 \times 10^{-4}$ rad m^{-1} (top) and $k = 1.5 \times 10^{-3}$ rad m^{-1} (bottom).

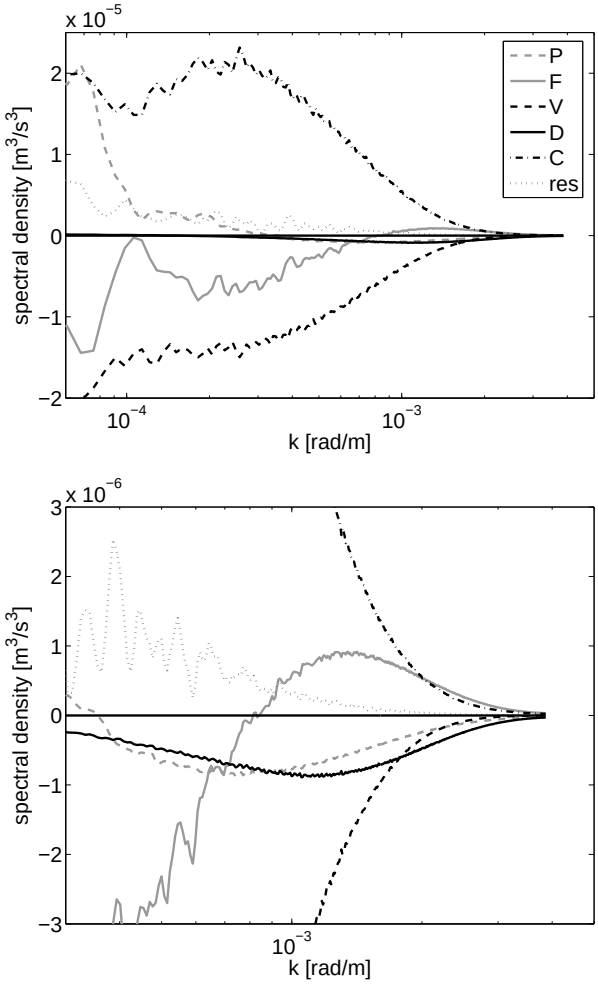

Figure 3: Spectral KE balance as a function of $k = |\mathbf{k}_h|$. The plotted terms are F (solid gray), P (dashed gray), C (dotted-dashed black), V (dashed black), D (solid black) and residual (dotted gray). Note the restrictions to the overall submesoscale range (top) and even finer (bottom).

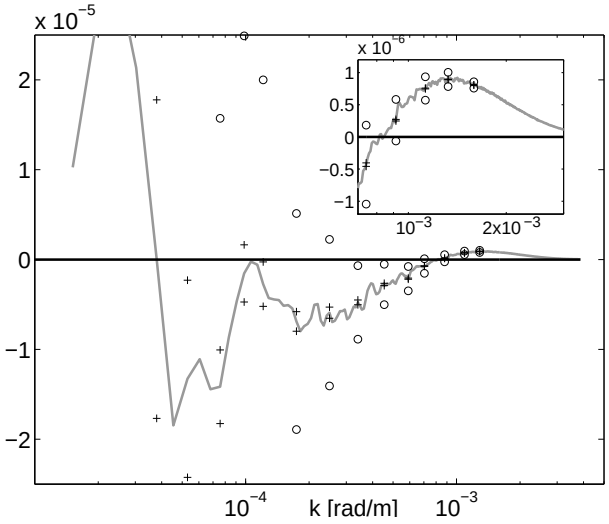

Figure 4: Sampling uncertainty in the spectral energy balance. Plotted is F (gray line), $F \pm$ its root-mean-square temporal variation (circles), and $F \pm$ the estimated sampling uncertainty (crosses) as defined in the text. The inset is an expanded view of the k range 7×10^{-4} rad m^{-1} $< k < 3 \times 10^{-3}$ rad m^{-1}, where F is changing sign and there is a forward KE cascade, $\Pi > 0$ (see Fig. 6).

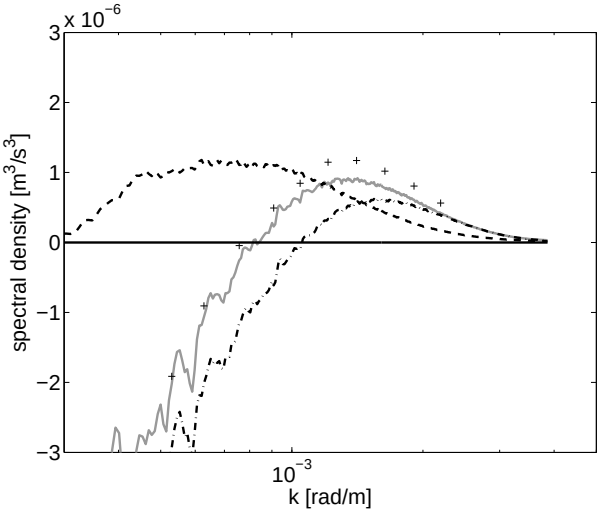

Figure 5: Spectral KE balance terms as a function of $k = |\mathbf{k}_h|$. Terms are F (solid gray), A_h (dotted-dashed black), and A_v (dashed black). The sum $A_h + A_v$ is indicated for some k values by $+$ symbols and should ideally coincide with F according to (4).

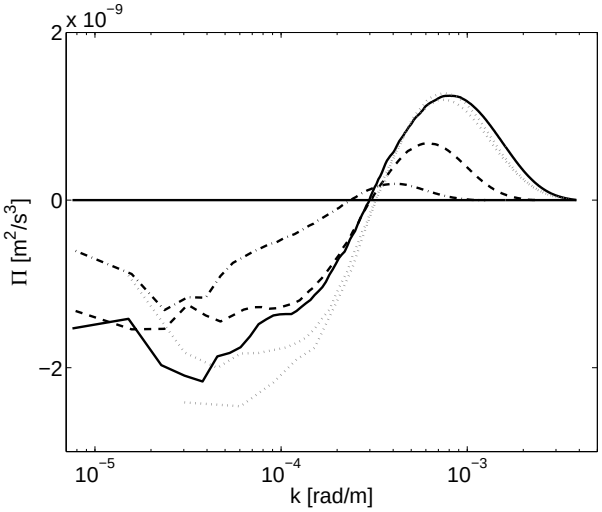

Figure 6: KE transfer function $\Pi(k)$ [m^2 s^{-3}]. Results are shown for simulations ICC3 with $dx = 3$ km (dot-dashed line), ICC1 with $dx = 1.5$ km (dashed line), and ICC0 with $dx = 0.75$ km (solid line) using a Hanning window. Also included are two estimates of $\Pi(k)$ (dotted line) for ICC0 obtained by evenly dividing the diagnostic domain into 4 and 16 sub-domains of sizes 384^2 and 192^2 grid points and averaging the resulting spectral fluxes.

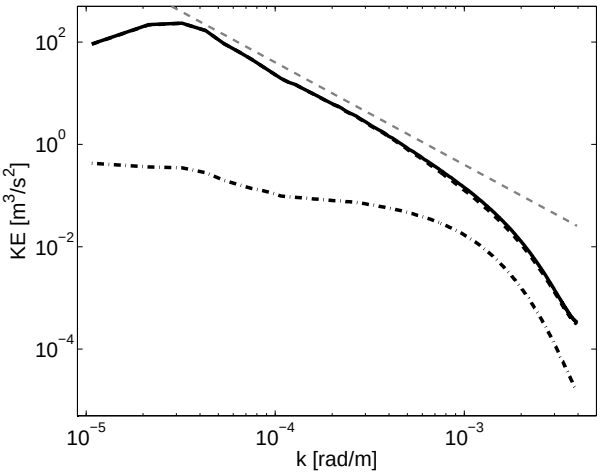

Figure 7: KE spectra at 10 m depth for the total horizontal velocity $\mathbf{u}_h$ (solid black line), its non-divergent component $\mathbf{u}_{hr}$ (dashed black line, almost indistinguishable from the solid line) and the sum of the spectra for the divergent component $\mathbf{u}_{hd}$ plus w (dot-dash black line). These spectra are calculated in the same way as in Fig. 1. The dashed gray line is $\propto k^{-2}$ for comparison.

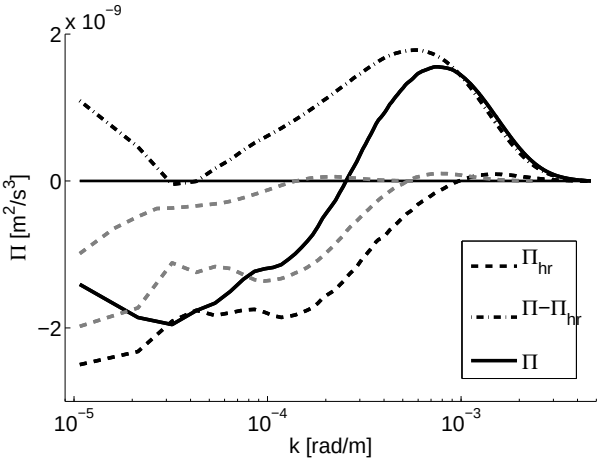

Figure 8: Spectral energy flux corresponding to the total horizontal velocity $\mathbf{u}_h$ (Π; solid line), horizontally non-divergent velocity $\mathbf{u}_{hr}$ (Π_{hr}; dashed line), and their difference (dot-dash line). Π_{hr} is represented for ICC0 (black) and ICC1 and ICC3 (gray; the range where $\Pi_{hr} > 0$ moves toward higher wavenumbers as resolution increases).

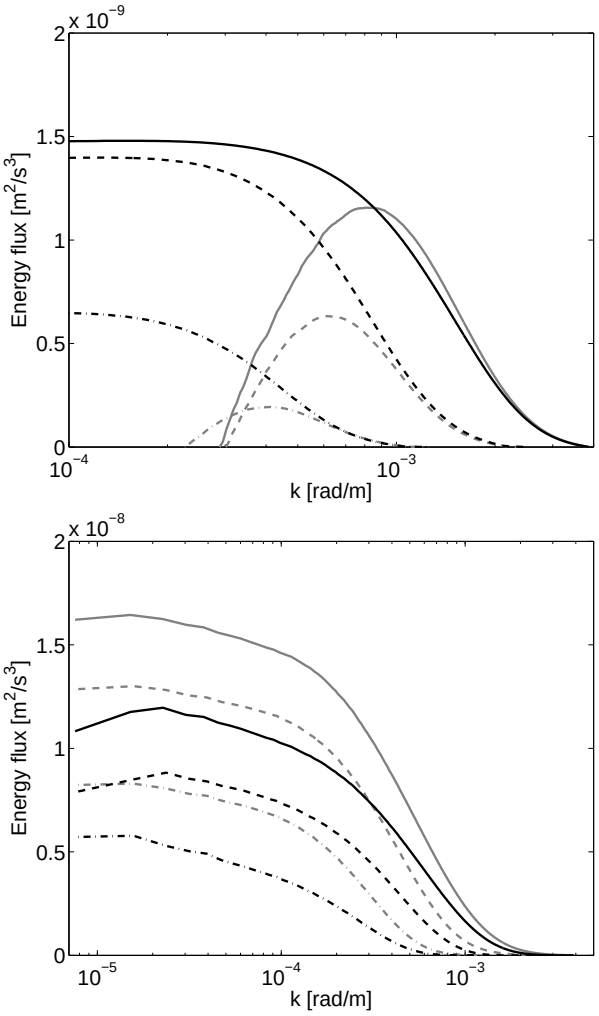

Figure 9: Top: KE transfer function $\Pi(k)$ in the range where it is positive (gray) and the negative of the integrated horizontal dissipation, $-\int_k^{k_{max}} R(k)\,dk$ (black). Bottom: Integrated potential energy conversion, $\int_k^{k_{max}} C(k)\,dk$ (gray) and the negative of vertical dissipation $-\int_k^{k_{max}} V(k)\,dk$ (black). Results are shown for simulations ICC3 with $dx = 3$ km (dot-dashed line), ICC1 with $dx = 1.5$ km (dashed), and ICC0 with $dx = 0.75$ km (solid). Units are [m^2 s^{-3}].

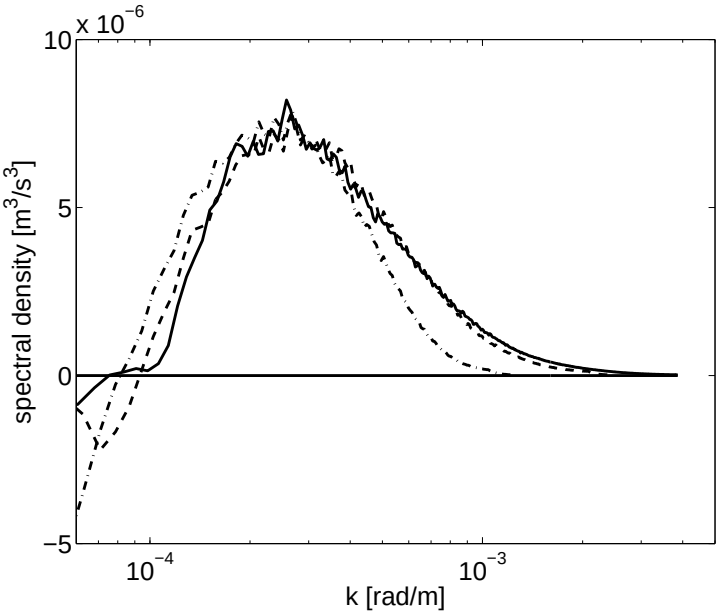

Figure 10: Spectral KE balance terms $C + V$ as a function of $k = |\mathbf{k}_h|$ for ICC0 (solid line), ICC1 (dashed), and ICC3 (dotted-dashed).

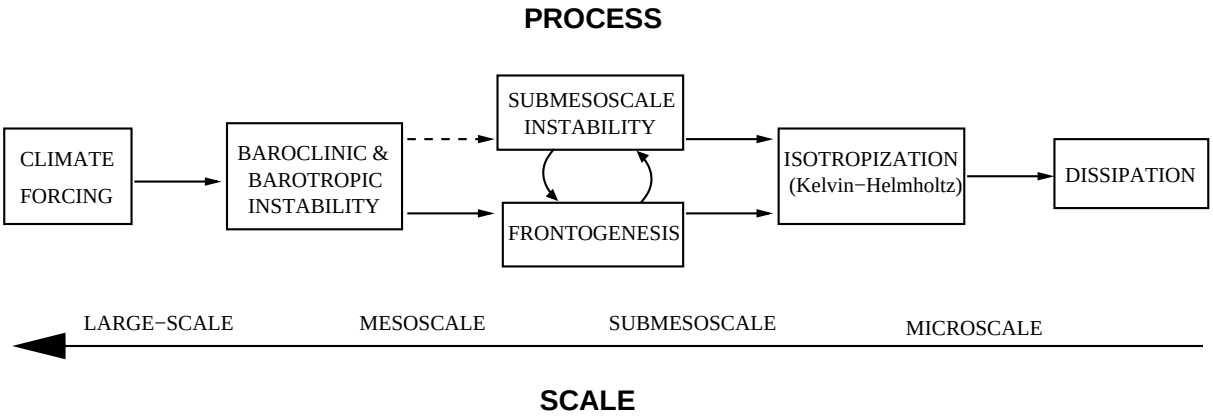

Figure 11: Schematic diagram for the important dynamical regimes by scale (bottom row) and their connecting total-energy transformation processes (top row) in an equilibrium oceanic circulation.

Table 1: Dynamical time scales [days] characterizing KE transfer (τ_A), dissipation (τ_D), and replenishment (τ_C) for several k values [rad m^{-1}]. The time scale is calculated by dividing the KE spectrum (Fig. 1) by either $A_h + A_v$, $R + V$, or C at a given k.

k	2×10^{-4}	4×10^{-4}	8×10^{-4}	1.6×10^{-3}
τ_A	8	5.6	6	0.4
τ_D	4.3	1.4	0.5	0.2
τ_C	3.3	1.0	0.3	0.3